IEEE Access
Multidisciplinary ⋮ Rapid Review ⋮ Open Access Journal

Received 17 May 2024, accepted 30 May 2024, date of publication 4 June 2024, date of current version 11 June 2024.

Digital Object Identifier 10.1109/ACCESS.2024.3409355

RESEARCH ARTICLE

Compact 8-Port 2 × 2 Array Based on Dual-Polarized Patch Antennas With Modified Cavity Field Distribution for Enhanced Port Isolation for 5G IoT Device MIMO Antennas

KIN-LU WONG[1,2], (Fellow, IEEE), YI-YANG HUANG[1], (Student Member, IEEE), AND WEI-YU LI[3], (Member, IEEE)

[1]Department of Electrical Engineering, National Sun Yat-sen University, Kaohsiung 80424, Taiwan
[2]6G Communication and Sensing Research Center, National Sun Yat-sen University, Kaohsiung 80424, Taiwan
[3]Information and Communications Research Laboratories, Industrial Technology Research Institute, Hsinchu 31057, Taiwan

Corresponding author: Kin-Lu Wong (wongkl@mail.nsysu.edu.tw)

This work was supported in part by the National Science and Technology Council, Taiwan, under Grant NSTC 113-2218-E-110-009.

ABSTRACT A compact 8-port 2 × 2 dual-polarized patch (DPP) antenna array with 8 uncorrelated waves for fifth-generation (5G) Internet-of-Things (IoT) device MIMO antennas in the n79 band (4.4-5.0 GHz) is presented. The 8-Port array has a small size of 51 mm × 51 mm or about $0.59\lambda^2$ with respect to the lower edge frequency (4.4 GHz) of the operating band. The equivalent size per port is $0.074\lambda^2$ only. The small 8-port array size is attributed to each DPP antenna therein with internal grounded metal rods added inside its resonant cavity and additionally four such DPP antennas 90°-sequentially oriented to form the array. The cavity field distribution excited by two ports in each DPP antenna can be modified by the internal grounded metal rods to achieve enhanced port isolation of larger than 15 dB in the operating band. Furthermore, based on using four such DPP antennas 90°-sequentially oriented in the array, the isolation of any two ports in different DPP antennas spaced by a small distance (less than 0.2λ here) can also be larger than 15 dB, thereby achieving a compact 8-Port array. We further propose to apply it as 8 receive antennas in the IoT device or eXtended Reality (XR) device for receiving 4 spatial MIMO streams (8 × 4 MIMO) in the 5G n79 band to obtain high data throughput. In this study, the 8 × 4 MIMO system [the extreme receive antennas (ERA)-aided MIMO in which the receive antennas outnumber the spatial streams] can have a high data throughput of 3.9 Gbps with 100 MHz bandwidth only. That is, a high spectral efficiency of 39 bps/Hz is obtained, which is about 2.3 times that (about 16.7 bps/Hz) of the 4 × 4 MIMO system that has been reported. Details of the compact 8-port 2 × 2 DPP antenna array, the modified cavity field distribution technique for enhanced port isolation of the DPP antenna, and the 8 × 4 MIMO system testing in practical campus public indoor and outdoor scenarios are presented.

INDEX TERMS 5G IoT device antennas, mobile antennas, MIMO antennas, 8-port 2 × 2 arrays, dual-polarized patch (DPP) antenna arrays, n79 band (4.4.-5.0 GHz), 8 × 4 MIMO systems, extreme receive antennas (ERA)-aided MIMO systems.

The associate editor coordinating the review of this manuscript and approving it for publication was Claudio Curcio.

I. INTRODUCTION

The World Radiocommunication Conference 2023 (WRC-23) organized by the International Telecommunication Union

(ITU) recently identifies the frequency band 4.8-4.99 GHz to be new international mobile communication (IMT) band [1]. Additionally, the WRC-23 resolves to recommend an agenda to consider 4.4-4.8 GHz as additional IMT bands four years later in the WRC-27 [1]. The whole n79 band (4.4-5.0 GHz) [2] as IMT bands for fifth-generation (5G) or future mobile communication service is thus promising to be recognized by the ITU, the United Nations agency for information and communication technologies, in the year 2027.

It is also noted that the current 5G communication uses the 4 × 4 MIMO system to double the spectral efficiency as compared to the fourth-generation (4G) communication with the 2 × 2 MIMO system, thereby achieving increased data throughput. It has also been reported that the data throughput in the 3.5 GHz band with 100 MHz bandwidth for the 4 × 4 MIMO operation is about 1.67 Gbps (the spectral efficiency about 16.7 bps/Hz) [3]. By applying the 8 × 8 MIMO system, which is considered to be promising for future mobile communication service [4], [5], [6], the data throughput in the 7.1 GHz band with 100 MHz bandwidth can reach about 3.4 Gbps (the spectral efficiency about 34 bps/Hz) [5], [6]. That is, by applying 8 spatial streams, the obtained data throughput can be about 2 times that of applying 4 spatial streams (1.67 Gbps vs. 3.4 Gbps for a same 100 MHz bandwidth).

Recently, the 8 × 8 MIMO operation for the WiFi-6E application in the lower 6 GHz band (5.925-6.425 GHz) has also been studied [7]. The measured data throughput with 80 MHz bandwidth centered at 6.18 GHz for the 8 × 8 MIMO system is about 3.64 Gbps (spectral efficiency about 45.5 bps/Hz) [7]. The relatively higher spectral efficiency as compared to those (about 34 bps/Hz) obtained in [5] and [6] for the 8 × 8 MIMO system may be partly owing to the lower frequencies having relatively richer multipath propagation (6.18 GHz in [7] vs. 7.1 GHz in [5], [6]).

The richer multipath propagation in the MIMO system can lead to a higher system capacity, thereby making it capable of supporting the signal modulation of 256 Quadruple Amplitude Modulation (QAM) with 8 bits per symbol in [7] as compared to the signal modulation of 64 QAM with 6 bits per symbol in [5] and [6].

Accordingly, we may expect the operating frequencies in the n79 band (4.4-5.0 GHz) have even richer multipath propagation than the frequencies in the lower 6 GHz band for the MIMO system studied in [7]. However, lower operating frequencies will also result in an increased size for the MIMO antennas, especially for the extreme receive antennas (ERA)-aided MIMO system [8], [9] requiring that the receive antennas therein outnumber the spatial MIMO streams.

It has also been reported that the measured data throughput in the 7.1 GHz band with 100 MHz bandwidth for the 16 × 8 MIMO system (16 receive antennas for 8 spatial streams) is about 5.6 Gbps (spectral efficiency about 56 bps/Hz or spectral efficiency per stream about 7 bps/Hz) [8], [9]. The corresponding spectral efficiency of the 16 × 8 MIMO system experienced by the user with the mobile device at the receiver side is much larger than those (34 bps/Hz or 45.5 bps/Hz) obtained in [5], [6], and [7] for the 8 × 8 MIMO system.

For the related ERA-aided MIMO system application in the n79 band (4.4-5.0 GHz), we propose in this study a compact 8-port 2 × 2 dual-polarized patch (DPP) antenna array as 8 receive antennas in the Internet-of-Things (IoT) device [10] or eXtended Reality (XR) device [11], [12] to obtain high data throughput for the 8 × 4 MIMO operation (8 receive antennas for 4 spatial streams). We obtain here that the measured data throughput in 4.8-4.9 GHz with 100 MHz bandwidth in the n79 band reaches 3.897 Gbps (spectral efficiency 38.97 bps/Hz) for the 8 × 4 MIMO system.

It is thus worth noting that the obtained spectral efficiency per stream reaches 9.74 bps/Hz for the 8 × 4 MIMO system in this study, which is much larger than that (7 bps/Hz per stream) obtained for the 16 × 8 MIMO system [8], [9]. The receive antennas are two times the spatial streams in both MIMO systems. The obtained results show that the ERA-aided MIMO is more effective for the case with 4 spatial streams than the case with 8 spatial streams. This may be because the former (4 spatial streams) is much less complicated in the MIMO system architecture than the latter (8 spatial streams). Therefore, the ERA-aided MIMO shows more prominent effects on the MIMO system with 4 spatial streams.

In addition, our proposed 8-port 2 × 2 array has a small size of $0.59\lambda_g^2$ [λ_g is the guided wavelength of the lower edge frequency (4.4 GHz) of the n79 band]. The lower edge frequency of the operating band generally dominates the required antenna size. The equivalent size per port is $0.074\lambda_g^2$ only. The small array size is attributed to each DPP antenna therein with internal grounded metal rods added inside its resonant cavity and additionally four such DPP antennas 90°-sequentially oriented to form the array.

The grounded metal rods can adjust the excited cavity field distribution of the two ports in each DPP antenna so that their port isolation can be larger than 15 dB over the target operating band. This is because the cavity field distribution can be adjusted such that each port is at around the null electric fields of the resonant mode excited by the other port over the operating band. In this case, enhanced isolation of the two ports in each DPP antenna can be obtained. Also, no external decoupling element (such as the L-shape metal wall in [7]) is needed, which can lead to a compact structure of the DPP antenna with enhanced port isolation.

For the 90°-sequential orientation [7], it can allow the isolation of any two ports in different DPP antennas spaced by a small distance (less than $0.2\lambda_g$ here) to be larger than 15 dB over the operating band. The compact 8-port array is therefore obtained in this study.

Related 8-port 2 × 2 DPP antenna arrays providing 8 MIMO antennas for the WiFi access-point applications have also been reported [7], [13]. The DPP antenna array

TABLE 1. Comparison of the compact 8-port 2 × 2 DPP antenna array for IoT device MIMO antennas (this work) with the reported 8-port 2 × 2 DPP antenna arrays for 2.4 GHz WiFi [13] or 5.925-6.425 GHz WiFi-6E [7] access-point applications. They are all in the form of patch antenna structures and suitable for on-metal surface applications.

[Reference]	[13]	[7]	This work
Operating band, fractional bandwidth for 8 ports	2.4-2.5 GHz, 4.1%	5.9-6.5 GHz, 9.7%	4.4-5.0 GHz, 12.8%
Array substrate's relative permittivity	About 2.3	Close to 1, about 1.07	Close to 1, about 1.05
Array height in guided wavelength (λ_g)	4.762 mm ($0.058\lambda_g$@2.4GHz)	5.0 mm ($0.10\lambda_g$@5.9GHz)	6.5 mm ($0.097\lambda_g$@4.4GHz)
Array size in guided wavelength (λ_g)	97.2 x 97.2 mm^2 ($1.39\lambda_g^2$@2.4GHz)	40 x 40 mm^2 ($0.66\lambda_g^2$@5.9GHz)	51 x 51 mm^2 ($0.59\lambda_g^2$@4.4GHz)
Equivalent size per port	$0.17\lambda_g^2$@2.4GHz	$0.083\lambda_g^2$@5.9GHz	$0.074\lambda_g^2$@4.4GHz
Patch edge-to-edge spacing	25.2 mm ($0.30\lambda_g$@2.4GHz)	11 mm ($0.22\lambda_g$@5.9GHz)	13 mm ($0.19\lambda_g$@4.4GHz)
Minimum port isolation in operating band	15 dB	20 dB	15 dB
For access points or IoT/XR devices	For WiFi access points	For WiFi-6E access points	For IoT/XR devices
External decoupling network; decoupling effects on antenna radiation	Yes, Decoupling network size 180 x 180 mm^2 ($4.8\lambda_g^2$@2.4GHz)	No, Port isolation enhanced by using metal wall-clad DPP antennas; stronger effects on antenna's radiation patterns	No, Port isolation enhanced by modifying cavity field distribution of DPP antennas; less effects on antenna's radiation patterns
Measured throughput and spectral efficiency (public indoor scenario)	------	3.64 Gbps (80 MHz bandwidth) and 45.5 bps/Hz (8 x 8 MIMO, 8 Rx antennas for 8 streams)	3.897 Gbps (100 MHz bandwidth) and 38.97 bps/Hz (8 x 4 MIMO, 8 Rx antennas for 4 streams)
Spectral efficiency per stream (public indoor scenario)	------	5.7 bps/Hz	9.74 bps/Hz

in [7] operates in 5.9-6.5 GHz (fractional bandwidth about 9.7%) with an equivalent array size per port of about $0.083\lambda_g^2$.

On the other hand, the DPP antenna array in [13] operates in 2.4-2.5 GHz (fractional bandwidth about 4.1%) with a larger array size per port of about $0.17\lambda_g^2$. The array size per port ($0.074\lambda_g^2$) of the proposed 8-port 2 × 2 DPP antenna array is smaller than those reported in [7] and [13]. The proposed 8-port array also shows a wider operating bandwidth (12.8% here vs. 9.7% in [7] or 4.1% in [13]).

It is also noted that for enhanced port isolation, an external decoupling network is needed in [13], while each DPP antenna is clad with an L-shape metal wall in [7]. The former [13] leads to a complicated 2 × 2 DPP antenna array structure. For the latter [7], owing to the L-shaped metal wall very close to each DPP antenna, the antenna's radiation pattern is affected to show an increased antenna gain (maximum antenna gain larger than 9 dBi in the operating band). In this case, the antenna's radiation pattern will have a narrower beamwidth, which will result in less rich multipath propagation for the MIMO system.

On the other hand, the proposed 8-port 2 × 2 DPP antenna array in this study uses a different decoupling technique of modifying the cavity field distribution of the DPP antenna therein. The radiation pattern of each DPP antenna is generally less affected.

In this case, the maximum antenna gain of the proposed design is less than 7 dBi over the operating band (see later in Section IV for the fabricated 8-port 2 × 2 array). In this case, the antenna's radiation patterns can be relatively wider, which is expected to have a relatively richer multipath propagation for the MIMO system. This will be advantageous for the MIMO system application.

The above discussion on the proposed design (this work) for IoT device MIMO antennas compared with the reported 8-port 2 × 2 DPP antenna arrays for 2.4 GHz WiFi [13] or 5.925-6.425 GHz WiFi-6E [7] access-point applications is also provided in Table 1. The antennas in Table 1 are all in the form of patch antenna structures and suitable for on-metal surface applications.

Some related works are also noted [14], [15], [16], [17]. Reference [14] reports a reconfigurable MIMO monopole antenna array with an electromagnetic band gap structure for 5G applications; and [15] reports ultra-wideband MIMO monopole antennas for the 5G mmWave application. The latter [15] is not suitable for 5G sub-6 GHz MIMO applications. Additionally, both References [14] and [15] are

in the form of monopole antennas and are not suitable to be directly mounted on metal surfaces.

As for [16], it introduced a decoupling and matching network for dual-band MIMO monopole antennas. The decoupling and matching network however will complicate the MIMO antenna structure. Reference [17] introduced a hybrid network consisting of a decoupling feed network and a defected ground network, which also complicates the MIMO antenna structure. Both designs in [16] and [17] are also not suitable to be directly mounted on metal surfaces. On the other hand, the three antennas (this work, [7], [13]) listed in Table 1 are in the form of patch antenna structure and are suitable for on-metal surface applications.

To summarize the advances of this study, the proposed design uses a new modified cavity field distribution technique for enhanced port isolation and requires no external decoupling network to achieve a simpler yet compact array structure. The proposed design has also been applied in practical campus public indoor and outdoor scenarios to successfully demonstrate its capability for 8 × 4 MIMO system applications. A high data throughput with the corresponding spectral efficiency per stream as high as 9.74 bps/Hz has been obtained, which to our best knowledge is the highest for the MIMO system with 4 spatial streams that have been reported.

In this study, to address the proposed compact 8-port 2 × 2 DPP antenna array for IoT device MIMO antennas and its application for the 8 × 4 MIMO system to achieve a high spectral efficiency per stream, we present in the following sections the array structure in Section II; the design consideration and parametric study in Section III; the experimental study of the fabricated array in Section IV; the 8 × 4 MIMO system testing in campus public indoor and outdoor scenarios in Section V; and finally the conclusion in Section VI.

II. THE 8-PORT 2 × 2 ARRAY

Fig. 1 shows the geometry of the compact 8-port 2 × 2 array based on the DPP antennas with modified cavity field distribution for enhanced port isolation covering the n79 band (4.4-5.0 GHz). The top and side views are shown in Fig. 1(a) and the exploded view is given in Fig. 1(b). The array with Ports 1-8 is formed by four 2-port DPP antennas 90°-sequentially oriented with their top square patches (19 mm x 19 mm) printed on a 0.4 mm thick FR4 substrate (relative permittivity 4.4, loss tangent 0.02). The FR4 substrate is spaced 6.1 mm above a ground plane of size 70 mm x 70 mm. The array substrate thus has an effective relative permittivity of about 1.05 and a thickness of 6.5 mm, which is about $0.097\lambda_g$ with respect to the guided wavelength at 4.4 GHz.

The array size is 51 mm × 51 mm (about $0.59\lambda_g^2$) with a small patch edge-to-edge spacing of 13 mm (about $0.19\lambda_g$) between adjacent DDP antennas. Each DPP antenna has two ports located at adjacent patch corners to excite two orthogonal half-wavelength resonant modes along the patch's

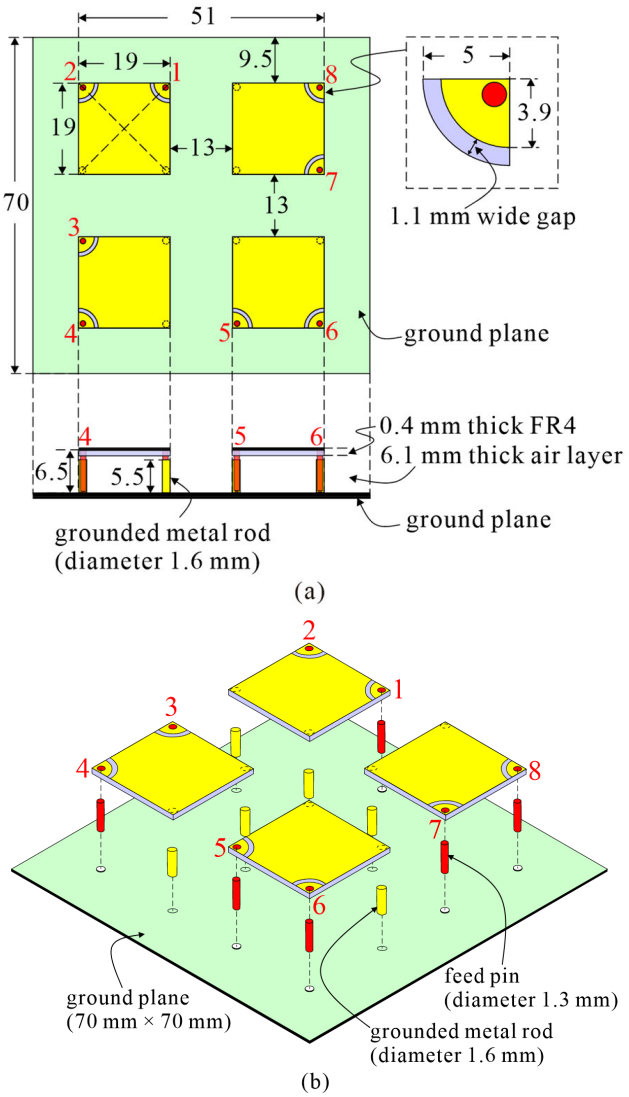

FIGURE 1. Geometry of the compact 8-port 2 × 2 array (Ports 1-8) based on dual-polarized patch (DPP) antennas with modified cavity field distribution for enhanced port isolation covering 4.4-5.0 GHz band (n79 band). (a) Top and side views. (b) Exploded view.

two diagonal lines. The excited resonant modes cover the n79 band.

It is worth noting that, with the 90°-sequential orientation [7], of the four DPP antennas in the array, the distance of two ports in adjacent DPP antennas can be maximized, which can help to obtain enhanced port isolation of larger than 15 dB for the case with a small element spacing of 13 mm here.

Also note that each port in the array is connected to a feed pin of length 6.5 mm and diameter 1.3 mm and is fed through a SMA connector placed behind the ground plane. To compensate for the introduced inductive reactance of the long feed pin, each port is capacitively coupled to the top square patch through a quarter-ring gap of width 11 mm.

Additionally, it is observed that there are some distortions in the cavity field distributions of the half-wavelength resonant modes excited by the two ports in each DPP antenna.

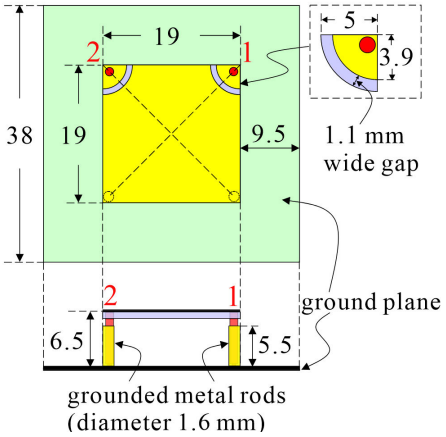

FIGURE 2. Geometry of the 2-port DPP antenna with two internal grounded metal rods to modify the cavity field distributions of two half-wavelength modes excited by Ports 1 and 2 at two adjacent patch corners.

This behavior is mainly owing to the presence of the long feed pin of the second port, when the first port is excited; and vice versa. This behavior has also been observed for the two-port same-polarized patch antenna studied in [18].

Because of the distortion in the excited cavity field distribution, the isolation of the two ports in each DPP antenna over the operating band is degraded. By introducing two grounded metal rods (height 5.5 mm, diameter 1.6 mm) at two opposite cavity corners facing the two ports, we can modify the cavity field distribution so that enhanced port isolation of the two ports in each DPP antenna is obtained.

This behavior will be analyzed in more detail for the DPP antenna standalone (the 2-port DPP antenna) mounted on a ground plane of size 38 mm x 38 mm (see Fig. 2). Except for different ground plane sizes, the dimensions of the 2-port DPP antenna in Fig. 2 are same as the corresponding ones of the 8-port 2 × 2 array in Fig. 1.

The simulated S parameters of both 8-port 2 × 2 array and 2-port DPP antenna are first studied. We apply the three-dimensional (3D) High Frequency Electromagnetic Simulation Software (HFSS) version 19.1 [19] in the simulation study. For the array, the simulated reflection coefficients of Ports 1 and 2 are given in Fig. 3(a). The S_{11} and S_{22} indicate that the desired resonant mode is excited with good impedance matching and covers 4.4-5.0 GHz. Note that the excited mode is the half-wavelength resonant mode resonated mainly along the patch's diagonal line.

There is also slight difference in the S_{11} and S_{22}, mainly because Port 1 is located within the array and Port 2 is at the array corner; thus, they will experience different coupling to other ports in the array. In addition, for Ports 3-8, their simulated reflection coefficients are same as those of Ports 1 and 2, mainly because the 8-port array has a symmetric structure. For brevity, those for Ports 3-8 are not presented.

The transmission coefficients of Port 1 to Ports 2-4 (S_{12}, S_{13}, S_{14}) and Port 1 to Ports 5-8 (S_{15}, S_{16}, S_{17}, S_{18}) are respectively shown in Fig. 3(b) and (c). The S_{12} has a dip at

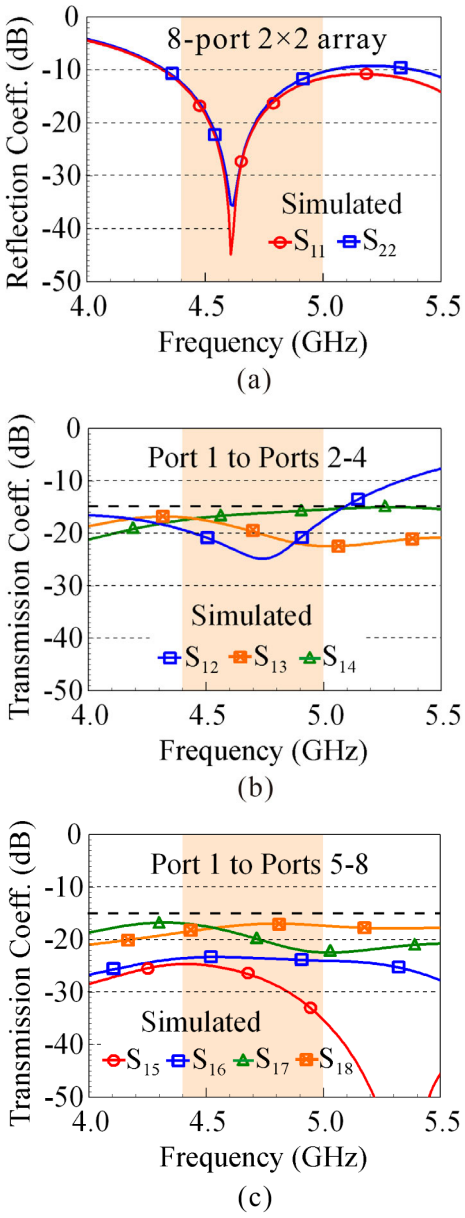

FIGURE 3. Simulated S parameters of the 8-port 2 × 2 array. (a) Reflection coefficients of Ports 1 and 2. (b) Transmission coefficients of Port 1 to Ports 2-4. (c) Transmission coefficients of Port 1 to Ports 5-8.

around the center frequency of the n79 band [see Fig. 3(b)], which is adjusted owing to the added internal grounded metal rods. Among the transmission coefficients, the S_{14} for Ports 1 to 4 is the largest at around 5.0 GHz, which is largely related to the excited resonant modes of Ports 1 and 4 are with parallel polarizations, although they are located in different DPP antennas and have a larger distance in the array.

However, the S_{14} is still less than −15.5 dB over the operating band. On the other hand, the S_{13} is less than −17 dB across the band, better than the S_{14}. This is largely because the excited resonant modes of Ports 1 and 3 are with orthogonal polarizations, although they have a smaller distance than that of Ports 1 and 4.

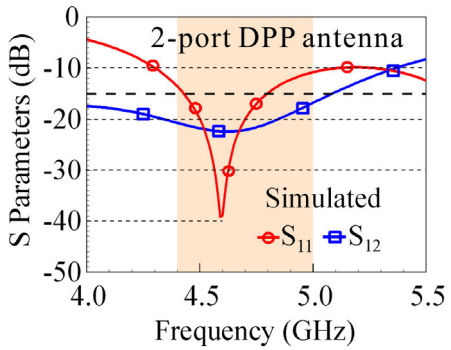

FIGURE 4. Simulated S parameters of the 2-port DPP antenna.

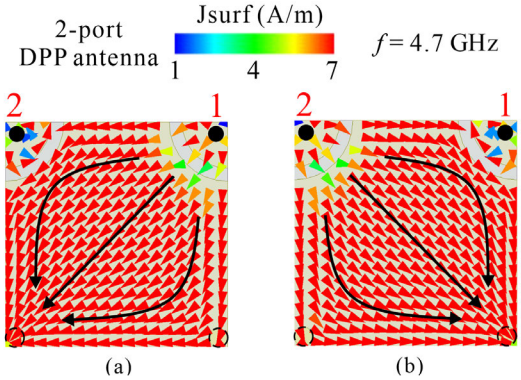

FIGURE 5. Simulated surface current distribution excited in the top patch of the 2-port DPP antenna at 4.7 GHz. (a) Port 1 excitation. (b) Port 2 excitation.

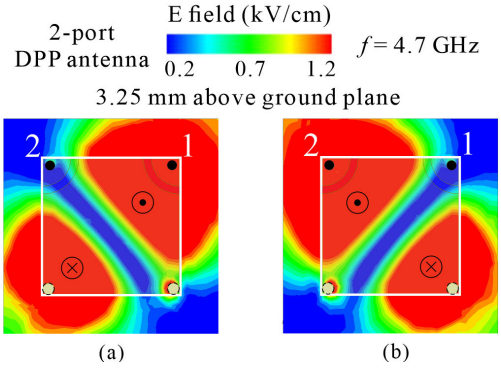

FIGURE 6. Simulated electric field distribution excited in the median plane (3.25 mm above the ground plane) of the resonant cavity of the 2-port DPP antenna at 4.7 GHz. (a) Port 1 excitation. (b) Port 2 excitation.

On the other hand, as seen in Fig. 3(c), the S_{15} and S_{16} are less than −24 dB, which may be simply that Port 1 to Ports 5 and 6 in the opposite DPP antenna have longer distances as compared to Port 1 to other ports. For the S_{17} and S_{18} (Ports 7 and 8 in the adjacent DPP antenna with respect to Port 1), they show similar trends as the S_{13} and S_{14} (Ports 3 and 4 also in the adjacent DPP antenna). Note that, in the 2 × 2 array, there are no additional decoupling elements added between the DPP antennas therein, although a compact array size is obtained.

In addition, for the MIMO antenna applications for IoT mobile devices or XR devices, the obtained transmission coefficients or the port isolation is considered to be sufficient to be applied as receive antennas in the MIMO system [5], [20], [21], [22]. The 8 × 4 MIMO system testing results will be presented in Section V.

For comparison, Fig. 4 shows the simulated S parameters of the 2-port DPP antennas. The S_{11} and S_{12} are very similar to the corresponding S parameters of the 8-port 2 × 2 array in Fig. 3(a) and (b). Therefore, one can conveniently apply the 2-port DPP antenna to form the proposed compact 8-port 2 × 2 array, without the need of fine-adjusting the dimensions of the DPP antennas and/or adding additional decoupling elements in the array. This also suggests that the DPP antenna standalone and the case with nearby three DPP antennas in the array have generally same antenna performance. Thus, in Figs. 5 and 6 for analyzing the excited resonant modes, the results for the 2-port DPP antenna are presented.

Fig. 5 shows the simulated surface current distribution excited in the top patch of the 2-port DPP antenna at 4.7 GHz, the center frequency of the operating band. For Port 1 excitation in Fig. 5(a), the surface currents are mainly excited along the diagonal line facing Port 1. Similarly, the surface currents excited by Port 2 are also mainly along the diagonal line facing Port 2. That is, the excited resonant modes of Ports 1 and 2 are mainly with orthogonal polarizations [23], [24].

Fig. 6 shows the simulated electric field distribution excited in the median plane (3.25 mm above the ground plane) of the resonant cavity of the 2-port DPP antenna at 4.7 GHz. It is worth noting that, for Port 1 excitation in Fig. 6(a), the diagonal line orthogonal to the excitation direction of the resonant mode has a null electric field; and the electric fields on its two sides are of opposite phases.

This indicates that the half-wavelength resonant mode along the diagonal line is excited by Port 1. Moreover, Port 2 is in the null electric field of the resonant mode excited by Port 1. This leads to enhanced port isolation of the 2-port DPP antenna. Similar behavior of Port 2 excitation in Fig. 6(b) is observed. This is mainly owing to the two grounded metal rods added in the 2-port DPP antenna. Detailed effects of the grounded metal rods will be analyzed in Section III.

The simulated antenna efficiency of the 8-port 2 × 2 array and the 2-port DPP antenna is also presented in Fig. 7. The antenna efficiency of Ports 1 and 2 in Fig. 7(a) for the 8-port 2 × 2 array is lower by about 10% as compared to that of Port 1 in Fig. 7(b) for the 2-port DPP antenna. This is mainly related to the additional coupling of Port 1 or 2 to other 6 ports in the three nearby DPP antennas in the array. However, the antenna efficiency of the 8 ports in the array is all larger than 82% over the desired operating band.

Fig. 8 shows the simulated envelope correlation coefficients (ECC) of the 8-port 2 × 2 array. Representative ECC values of Port 1 to Ports 2-4 and to Ports 5-8 are respectively shown in Fig. 8(a) and (b). The simulated ECC is obtained by applying the three-dimensional far-field electric fields based

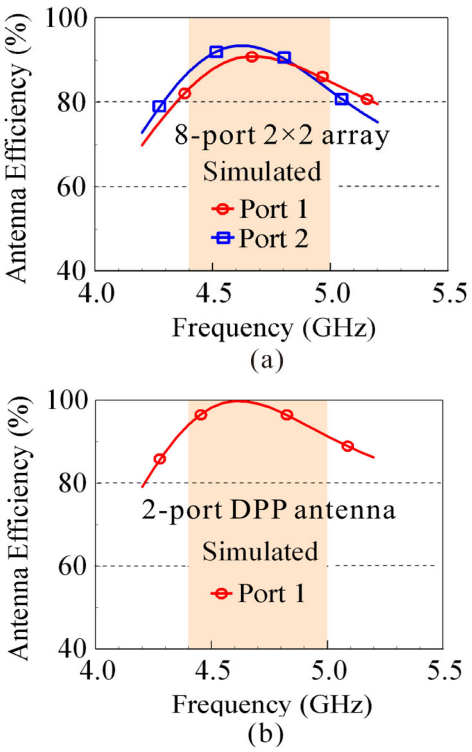

FIGURE 7. Simulated antenna efficiency. (a) Ports 1 and 2 in the 8-port 2 × 2 array. (b) Port 1 in the 2-port DPP antenna.

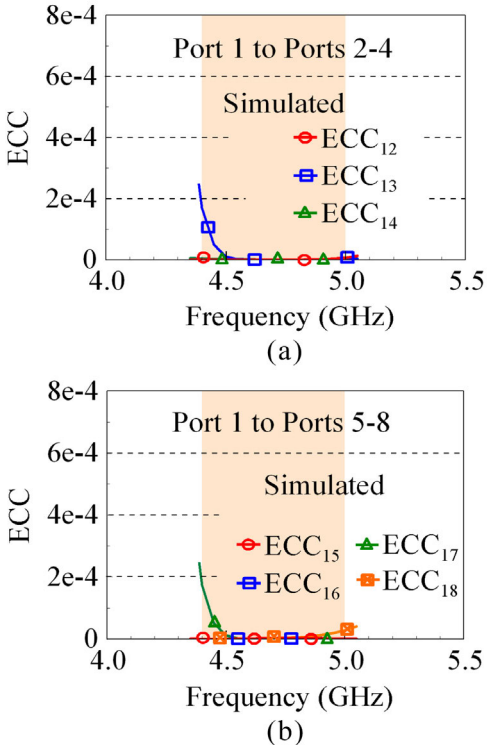

FIGURE 8. Simulated envelope correlation coefficients (ECC) of the 8-port 2 × 2 array. (a) Port 1 to Ports 2-4. (b) Port 1 to Ports 5-8.

expression [25]. Very low ECC values (less than 0.0002) over the operating band are obtained. The results indicate that the compact 8-port 2 × 2 array with a small array size can provide 8 uncorrelated waves for MIMO system applications.

III. OPERATING PRINCIPLE AND PARAMETRIC STUDY

Fig. 9 shows the geometry of the 2-port DPP antenna without the grounded metal rods (denoted as Design A). The dimensions of Design A are same as corresponding ones shown in Fig. 2. The simulated S parameters of Design A are presented in Fig. 10. The excited resonant mode or the S_{11} for Design A is slightly shifted to high frequencies, as compared to the results in Fig. 4 for the DPP antenna standalone.

Additionally, the S_{12} is shifted much further to higher frequencies. This makes the isolation of Ports 1 and 2 in the excited resonant mode degraded, although the two ports excite two orthogonally polarized resonant modes. This can be seen in Fig. 11, in which the excited surface currents of Ports 1 and 2 in Design A are generally orthogonal to each other, similar to the results in Fig. 5 for the DPP antenna standalone.

The degraded port isolation can be seen more clearly from the electric field distribution of Design A in Fig. 12. It is observed that the null electric field does not occur along the diagonal line orthogonal to the resonant direction of the excited resonant mode for both Port 1 and Port 2 excitation. When compared with the corresponding results in Fig. 6 for the DPP antenna with the grounded metal rods, we can see that the electric field in the opposite side of the excitation port

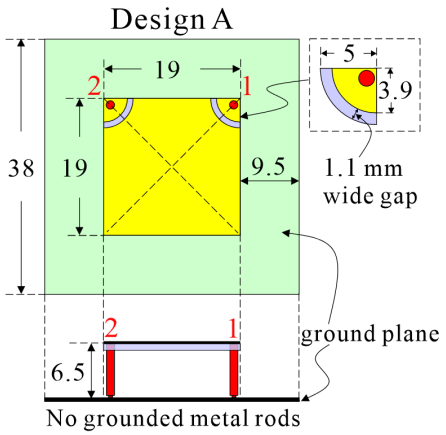

FIGURE 9. Geometry of the 2-port DPP antenna without the grounded metal rods (Design A). The dimensions of Design A are same as the corresponding ones shown in Fig. 2.

is much weaker than that near the excited port. This leads to quite asymmetric field distribution on the two sides of the null electric field of the excited resonant mode.

This behavior is mainly because, when Port 1 is excited, the long feed pin of Port 2 causes some distortion in the field distribution of the excited resonant mode. Similar behavior occurs when Port 2 is excited. The distortion in the field distribution in the resonant cavity between the top patch and the ground plane makes the null electric field of the excited resonant mode slightly shifted away from the diagonal line. Thus, when Port 1 at one patch corner is excited, Port 2 at the adjacent patch corner will no longer be within the null

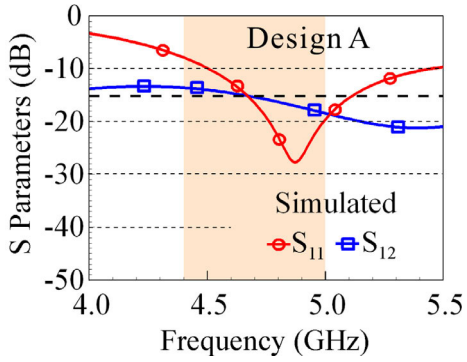

FIGURE 10. Simulated S parameters of Design A.

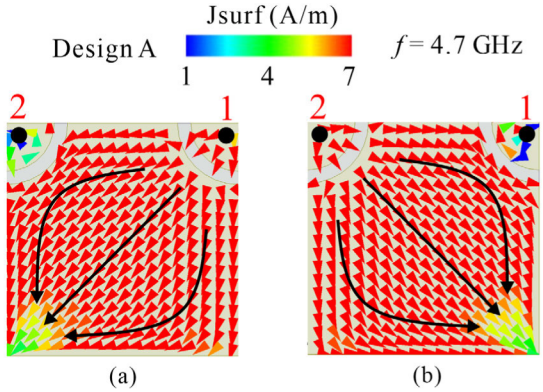

FIGURE 11. Simulated surface current distribution excited in the top patch of Design A at 4.7 GHz. (a) Port 1 excitation. (b) Port 2 excitation.

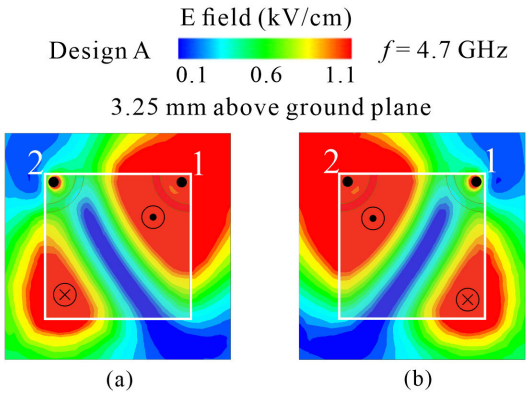

FIGURE 12. Simulated electric field distribution excited in the median plane (3.25 mm above the ground plane) of the resonant cavity of Design A at 4.7 GHz. (a) Port 1 excitation. (b) Port 2 excitation.

electric field region of the excited mode of Port 2; and vice versa. This will lead to increased coupling of Ports 1 and 2.

This phenomenon is alleviated by adding two grounded metal rods of length 5.5 mm at the other two patch corners of Design A. The metal rod is grounded to the ground plane and is spaced 1 mm to the top patch, as seen in Figs. 1 and 2. Owing to the small spacing between the grounded metal rods and top patch, there is increased electric field at the patch corners opposite to the ones located Ports 1 and 2.

In this case, more symmetric electric field distribution on the two sides of the null electric field of the excited resonant modes can be obtained (see Fig. 6). This will thus allow the

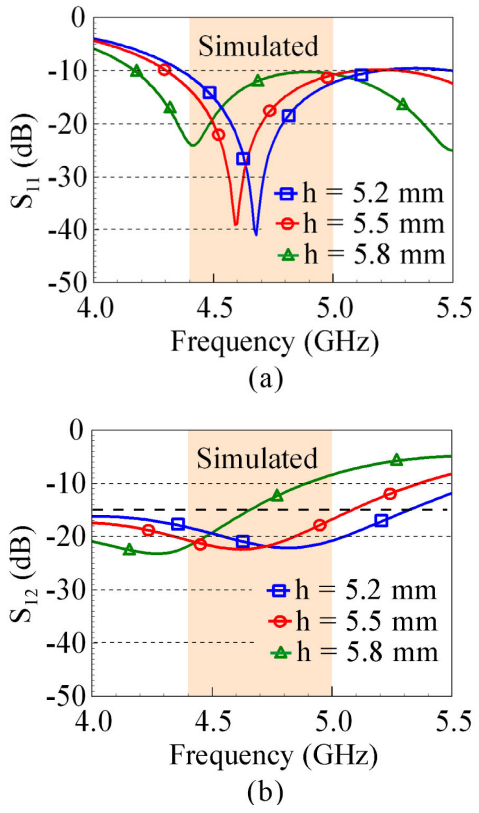

FIGURE 13. Simulated S parameters for varying the height (h) of the grounded metal rods in the 2-port DPP antenna. (a) The S_{11}. (b) The S_{12}.

null electric field of the excited modes to occur along the diagonal lines of the resonant cavity between the top patch and ground plane. In this case, enhanced port isolation of Ports 1 and 2 in the DPP antenna is obtained.

A parametric study of varying the height of the grounded metal rods in the 2-port DPP antenna is also conducted. Fig. 13 shows the simulated S parameters for varying the height (h) of the grounded metal rods from 5.2 mm to 5.8 mm. We can vary the height to adjust the S_{11} in Fig. 13(a) and the S_{12} in Fig. 13(b); thus, the excited resonant modes cover the desired operating band. Furthermore, enhanced port isolation is also obtained. In this study, the height h is selected to be 5.5 mm for the proposed design.

The patch edge-to-edge spacing (d) in the 2 × 2 array is also studied. Fig. 14 shows the simulated S parameters for varying the spacing from 11 mm to 15 mm. Fig. 14(a) shows that the S_{11} is almost not affected and the S_{12} is also slightly affected. The S_{13} and S_{14} are given in Fig. 14(b), the S_{15} and S_{16} are in Fig. 14(c), and the S_{17} and S_{18} are in Fig. 14(d). Note that, for a smaller spacing (d = 11 mm), the S_{14} becomes larger than −15 dB. In this case, although a smaller spacing can further decrease the array size, the spacing in the proposed design is chosen to be 13 mm.

IV. FABRICATED 8-PORT 2 × 2 ARRAY

The 8-port 2 × 2 array is fabricated and experimentally studied. Fig. 15 shows the fabricated prototype. Each port is connected to a SMA connector on the back side of the ground

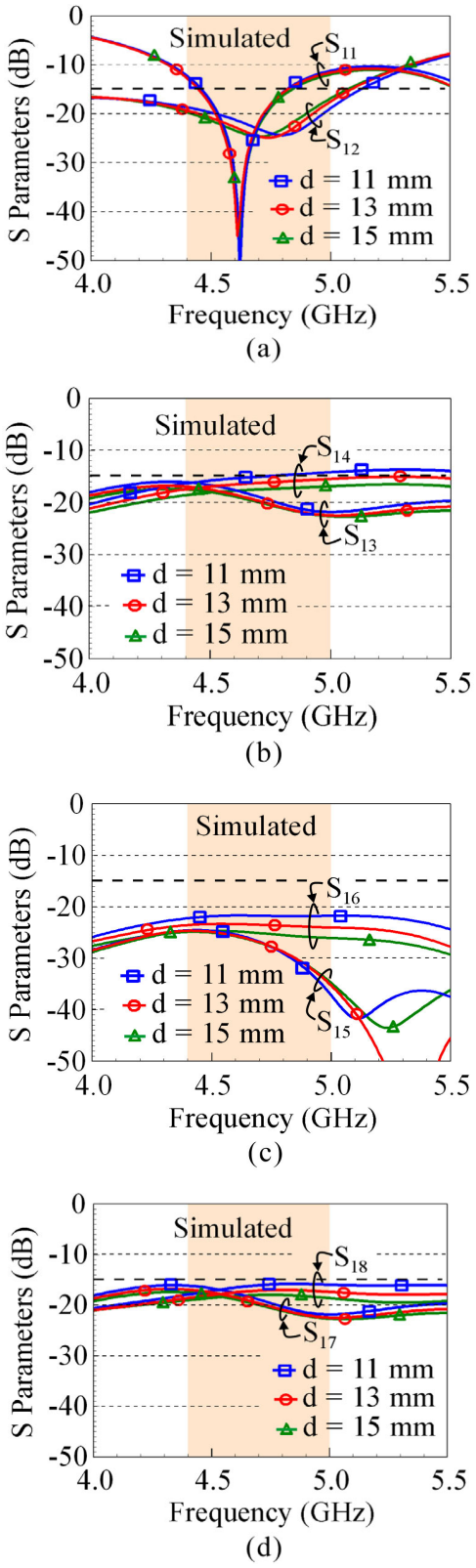

FIGURE 14. Simulated S parameters for varying the patch edge-to-edge spacing (d) of two adjacent DPP antennas in the 8-Port 2 × 2 array. (a) The S_{11}, S_{12}. (b) The S_{13}, S_{14}. (c) The S_{15}, S_{16}. (d) The S_{17}, S_{18}.

plane for excitation. The measured reflection coefficients of Ports 1, 3, 5, 7 (at each patch's inner corner and close

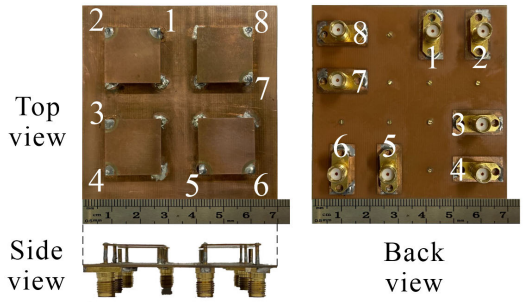

FIGURE 15. Fabricated 8-port 2 × 2 array.

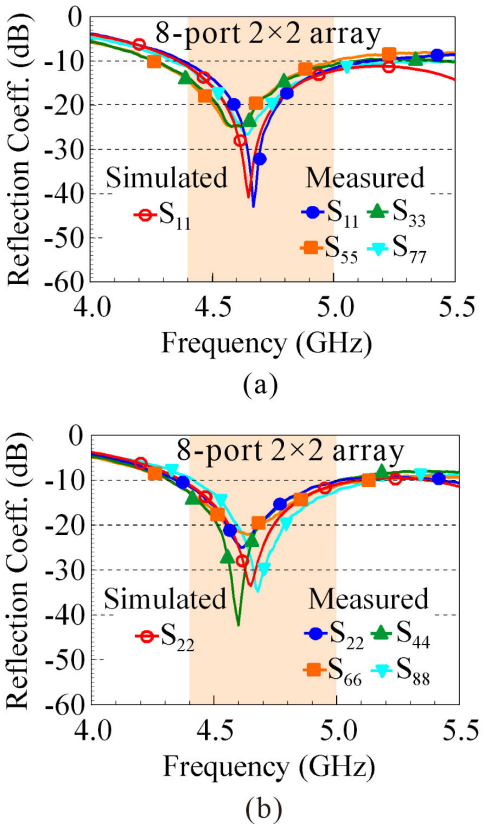

FIGURE 16. Measured reflection coefficients of the fabricated 8-port 2 × 2 array. (a) Ports 1, 3, 5, 7. (b) Ports 2, 4, 6, 8.

to adjacent DPP antennas) and Ports 2, 4, 6, 8 (at each patch's outer corner and also at array corners) are presented in Fig. 16(a) and (b), respectively. The corresponding simulated S_{11} and S_{22} are also given in the figure for comparison. The measured results generally conform to the simulated ones and cover 4.4-5.0 GHz.

Fig. 17 shows the measured transmission coefficients. Representative measured results of Port1 to Ports 2-8 are presented. The S_{12} and S_{13} are given in Fig. 17(a); the S_{14} and S_{15} are in Fig. 17(b); and the S_{16}, S_{17}, and S_{18} are in Fig. 17(c). From the measured results, the transmission coefficients over the operating band are all less than −15 dB; and the measured S_{15}, S_{16}, and most of the S_{12} are less than −20 dB in 4.4-5.0 GHz. The measured data also agree with the corresponding simulated results.

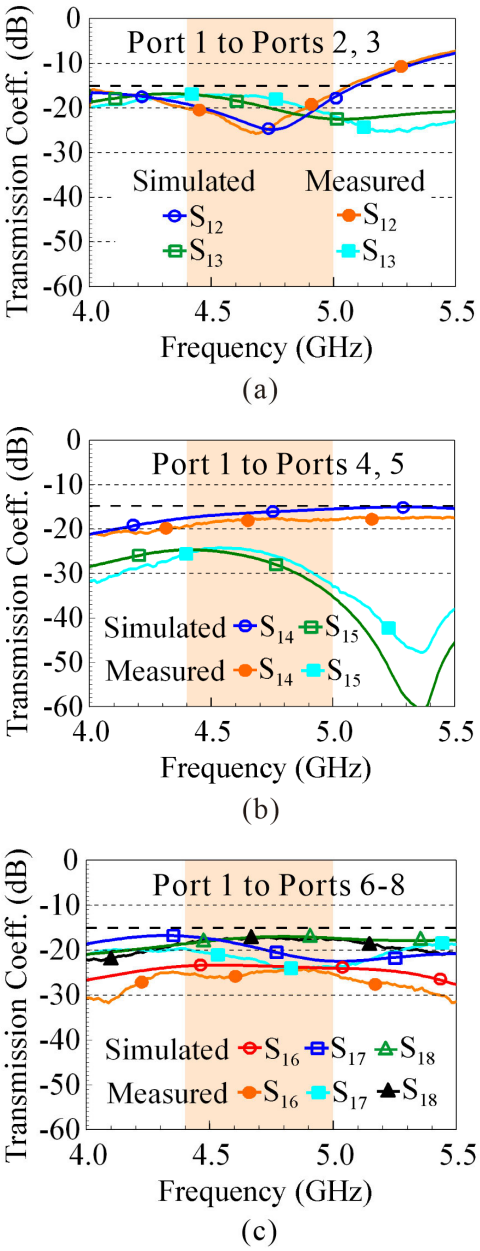

FIGURE 17. Measured transmission coefficients of the fabricated 8-port 2 × 2 array. (a) The S_{12}, S_{13}. (b) The S_{14}, S_{15}. (c) The S_{16}, S_{17}, S_{18}.

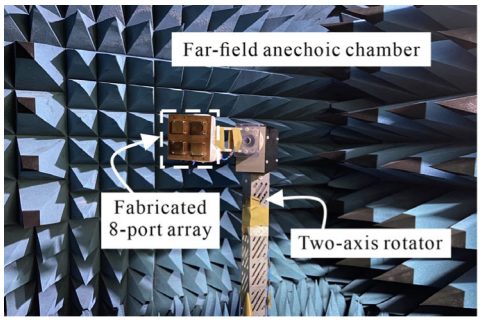

FIGURE 18. The fabricated 8-port 2 × 2 array measured in the far-field anechoic chamber.

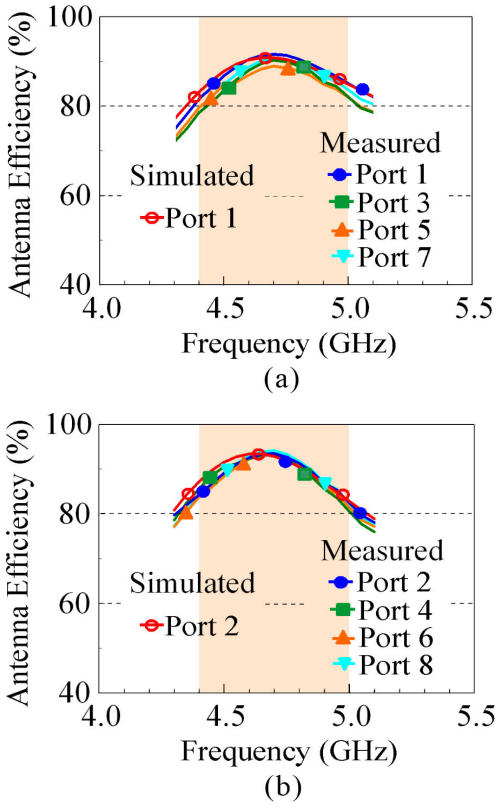

FIGURE 19. Measured antenna efficiency of the fabricated 8-port 2 × 2 array. (a) Ports 1, 3, 5, 7. (b) Ports 2, 4, 6, 8.

Fig. 18 shows the measurement setup of the fabricated 8-port 2 × 2 array in our far-field anechoic chamber for radiation performance study. The array is mounted on a two-axis rotator to rotate along two orthogonal (φ and θ) directions. The antenna's total radiation power for each port can therefore be obtained in the measurement (the Great circle test method [26]) and the antenna efficiency of Ports 1-8 is then evaluated.

Fig. 19(a) and (b) show the measured antenna efficiency respectively for Ports 1, 3, 5, 7 and Ports 2, 4, 6, 8. The measured antenna efficiency is larger than 78% (Ports 1, 3, 5, 7) or 80% (Ports 2, 4, 6, 8) in 4.4-5.0 GHz and also generally agrees with the simulated results. Note that Ports 2, 4, 6, 8 show slightly larger antenna efficiency, which is mainly because they are located at array corners and their coupling to other ports in the array is relatively not as strong as Ports 1, 3, 5, 7 to other ports.

The measured antenna gain for Ports 1-8 is provided in Fig. 20. The antenna gain of Ports 1, 3, 5, 7 is slightly varied around 6.0 dBi in 4.4-5.0 GHz [see Fig. 20(a)], while that of Ports 2, 4, 6, 8 shows relatively larger variations from about 5.0 dBi to 6.6 dBi [see Fig. 20(b)]. This is largely because Ports 2, 4, 6, 8 are at array corners and also close to two edges of the ground plane; they are thus more sensitive to the ground size variation in terms of the operating wavelength which decreases with increasing frequencies.

At higher frequencies, the effective ground size in terms of the wavelength is larger; thus, the antenna's radiation will be

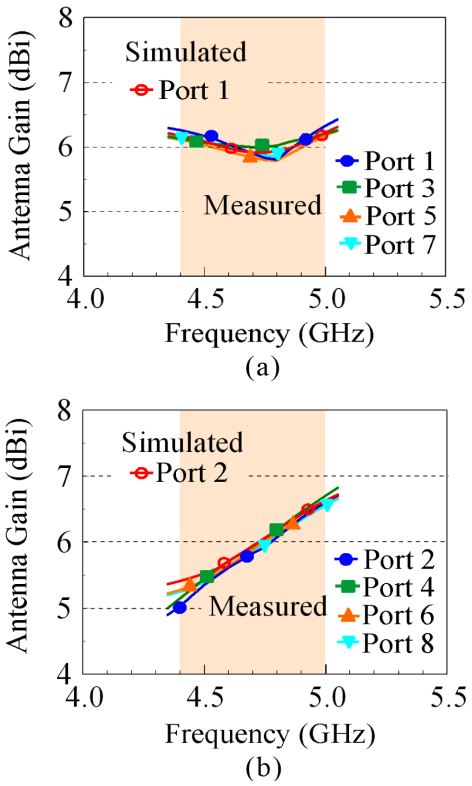

FIGURE 20. Measured antenna gain of the fabricated 8-port 2 × 2 array. (a) Ports 1, 3, 5, 7. (b) Ports 2, 4, 6, 8.

stronger in the front side of the ground plane than in the back side thereof. This leads to increasing antenna gain at higher frequencies, especially for Ports 2, 4, 6, 8 seen in Fig. 20(b). Also, it is seen that both the measured antenna efficiency and antenna gain generally conform to the simulated results which are included in the figure for comparison.

Note that the maximum antenna gain over the operating band is about 6.6 dBi only. On the other hand, the maximum antenna gain is larger than 9 dBi in the 2 × 2 DPP antenna array with the decoupling technique of the L-shape metal wall clad to each DPP antenna [7]. The smaller antenna gain is largely because the antenna's radiation pattern is less affected by the proposed modified cavity field distribution. This is expected to be advantageous to have richer multipath propagation for the MIMO system.

Fig. 21 shows the measured radiation patterns of Ports 1-8 in the fabricated array at 4.7 GHz. The radiation patterns of Ports 1, 3, 5, 7 and Ports 2, 4, 6, 8 are respectively plotted in Fig. 21(a) and (b). The radiation patterns in the $\varphi = 45°$ or 135° plane along the resonant direction of each port are presented. The measured and simulated radiation patterns are generally in agreement, and Ports 1-8 all show broadside radiation in the z direction ($\theta = 0°$).

The ECC results are then evaluated by using the measured three-dimensional far-field electric fields [21]. Fig. 22 shows the representative ECC values of Port 1 to Ports 2-8 for the fabricated 8-port 2 × 2 array. The ECC_{12} and ECC_{13} are given in Fig. 21(a); The ECC_{14} and ECC_{15} are in Fig. 21(b); and

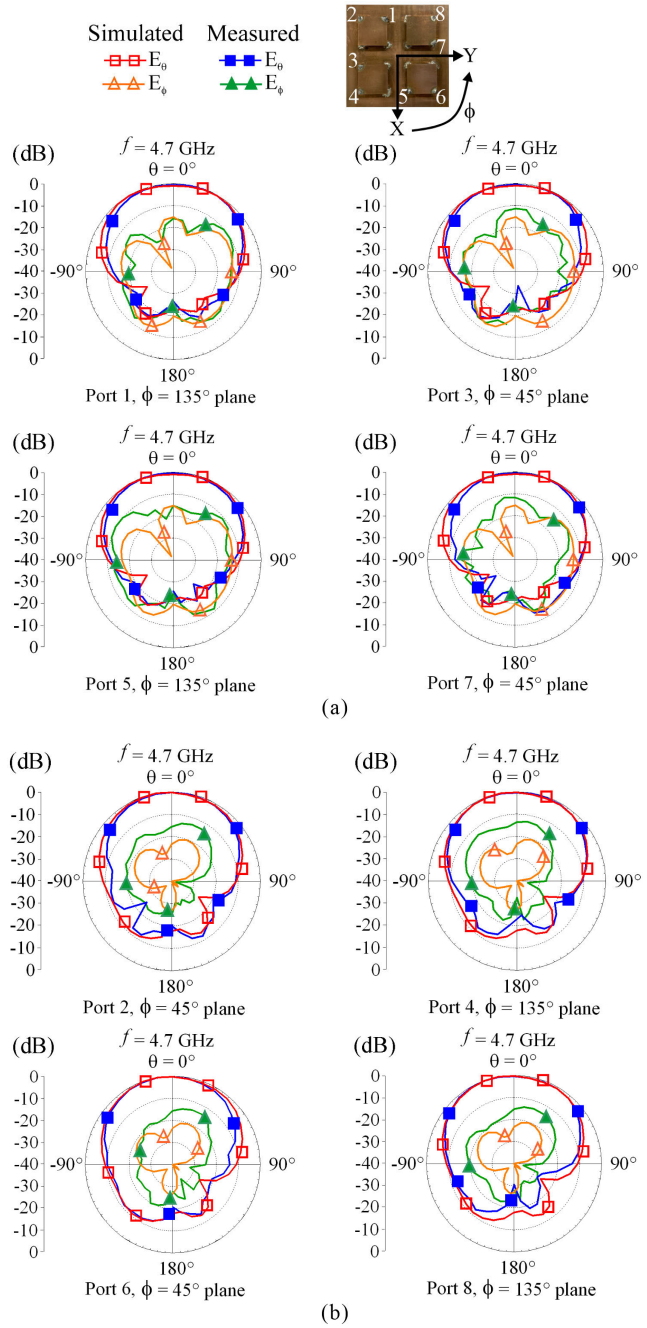

FIGURE 21. Measured radiation patterns of the fabricated 8-port 2 × 2 array. (a) Ports 1, 3, 5, 7. (b) Ports 2, 4, 6, 8.

The ECC_{16}, ECC_{17}, and ECC_{18} are in Fig. 21(c). The ECC_{mn} in the figure indicates the result for Port m and Port n. All the measured ECC values are less than 0.03 in 4.4-5.0 GHz.

Note that, due to the measurement limitation, the measured electric field amplitude and phase cannot be as accurate as the simulated results, which may make the obtained ECC values not as small as those shown in Fig. 8. However, the ECC values of less than 0.03 obtained here are low enough to be considered as uncorrelated for any two radiated waves in the MIMO system [5], [6], [7], [8], [9].

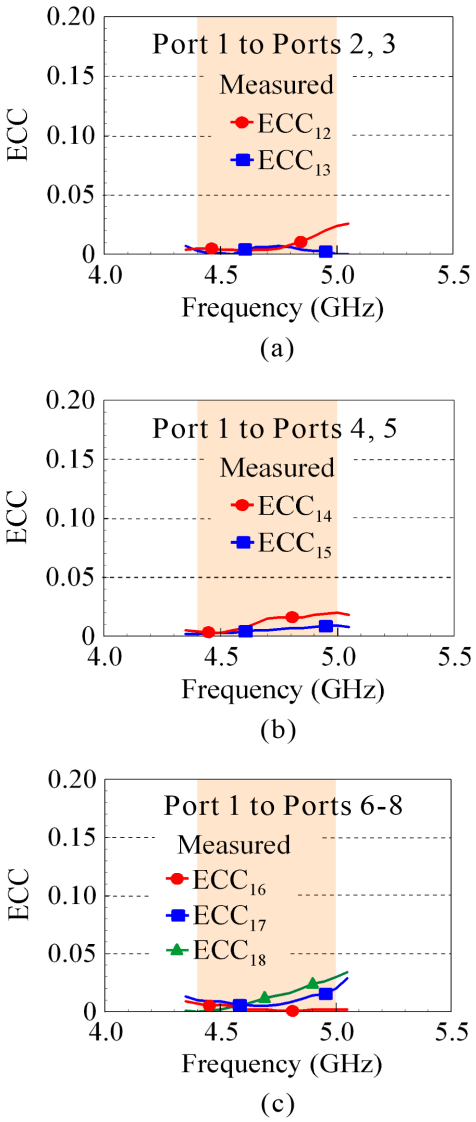

FIGURE 22. Measured envelope correlation coefficients of the fabricated 8-port 2 × 2 array. (a) The ECC_{12}, ECC_{13}. (b) The ECC_{14}, ECC_{15}. c) The ECC_{16}, ECC_{17}, ECC_{18}.

V. THE 8 × 4 MIMO SYSTEM TESTING

To test the capability of the compact 8-port array for practical MIMO system applications, we conducted the 8 × 4 MIMO system testing in both practical indoor and outdoor scenarios in the university campus. Fig. 23 shows the 8 × 4 MIMO system testbed [8 receive (Rx) antennas, 4 transmit (Tx) antennas] at National Sun Yat-sen University (NSYSU). The fabricated 8-port 2 × 2 DPP array in Fig. 15 is used as 8 Rx antennas at the receiver side. A 4-port single-patch antenna based on the design in [27] is fabricated and applied as 4 Tx antennas to transmit 4 spatial streams at the transmit side. The received signals of the 8 Rx antennas are fed into two 4-port high-performance oscilloscopes and then processed by the in-house developed software MIMO receiver [5], [6], [7], [8], [9], which is mainly based on 5G New Radio (NR) standard.

Fig. 24 shows the public indoor scenario (area 19 m × 6.6 m) inside the NSYSU electrical engineering department

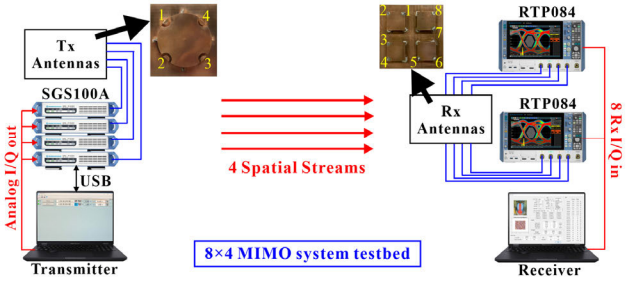

FIGURE 23. The 8 × 4 MIMO system testbed at National Sun Yat-sen University. The fabricated 8-port 2 × 2 DPP array in Fig. 15 is used as 8 receive (Rx) antennas at the receiver side. A 4-port single-patch antenna based on the design in [27] is fabricated and applied to transmit 4 spatial streams at the transmit side.

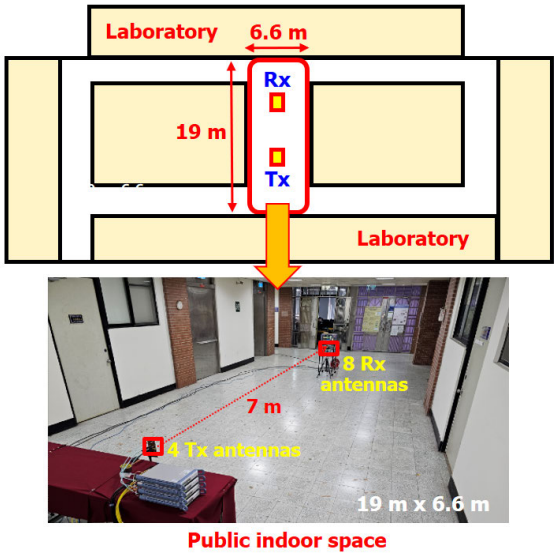

FIGURE 24. The public indoor scenario (area 19 m x 6.6 m) inside the NSYSU electrical engineering department building for the 8 × 4 MIMO systems testing.

building for the 8 × 4 MIMO system testing. The 8 Rx antennas and 4 Tx antennas are placed along the centerline of the public indoor space and spaced by a distance of 7 meters in the measurement. The frequency band of 4.8-4.9 GHz with 100 MHz bandwidth in the 79 band is tested; this frequency band has been assigned by the Taiwan government as a 5G band to use by the public and private sectors for special purposes [28].

Table 2 lists the measured 8 × 4 MIMO system performance in 4.8-4.9 GHz for the public indoor scenario. It is worth noting that the 8 × 4 MIMO system in the indoor scenario supports the signal modulations of 1024 QAM (10 bits per symbol) and 4096 QAM (12 bits per symbol). The measured signal noise ratios (SNR) of the 8 Rx antennas (Ports 1-8 of the fabricated 8-port array) are recorded. The average SNR of the 8 Rx antennas is around 29 dB.

For the 8 × 4 MIMO system, it is interesting to find that the measured MIMO capacity (obtained in the practical indoor scenario) is very close to the calculated MIMO capacity (obtained by assuming the MIMO environment with an ideally rich multipath condition). As listed in the table, for

TABLE 2. Measured 8 × 4 MIMO system performance for the campus public indoor scenario (Fig. 24).

f_0 = 4.85 GHz (4.8-4.9 GHz), Campus public indoor space (19 m x 6.6 m), Rx/Tx distance 7 m		
MIMO system, Signal modulation	8 x 4 MIMO, 1024 QAM	8 x 4 MIMO, 4096 QAM
Measured Signal Noise Ratio (dB) of 8 Rx antennas at the receiver side	30.7, 28.6, 28.7, 28.6 26.8, 29.5, 28.6, 28.8 (Average SNR ≈ 28.9 dB)	31.4, 28.9, 28.8, 29.0 26.6, 29.7, 28.6, 28.8 (Average SNR ≈ 29.2 dB)
Calculated MIMO Capacity (A) (Ideally rich multipath condition)	40.7 bps/Hz	40.9 bps/Hz
Measured MIMO Capacity (B)	40.6 bps/Hz	40.8 bps/Hz
MIMO Efficiency (B/A)	99.8%	99.8%
Uncoded Bit Error Rate	0.00012	0.010
Coded Bit Error Rate	0	0
Measured Throughput (T)	3281 Mbps	3897 Mbps
Spectral Efficiency (T/100 MHz)	32.81 bps/Hz	38.97 bps/Hz
Spectral efficiency per stream (public indoor scenario)	8.21 bps/Hz	9.74 bps/Hz

the 1024 QAM case, the calculated and measured MIMO capacities are respectively 40.7 bps/Hz and 40.6 bps/Hz for the average SNR about 28.9 dB; while for the 4096 QAM case, they are respectively 40.9 bps/Hz and 40.8 bps/Hz for the average SNR about 29.2 dB.

In this case, the obtained MIMO efficiency is about 99.8%, which indicates that the 8 × 4 MIMO system in the tested indoor scenario can be considered to have an almost ideally rich multipath condition.

This almost ideally rich multipath condition is related to the Rx antennas two times that of the spatial streams in the 8 × 4 MIMO system. This is equivalent to using two Rx antennas to receive one spatial stream. In this case, with the transmitted power fixed, the equivalent received power at the receiver for one spatial stream is however doubled. This can lead to an effective increase in the higher limit of the MIMO system capacity.

More importantly, the additional Rx antennas can also result in more additional multipath signals received by the receiver. The additional multipath signals can further result in an equivalently richer multipath environment for the MIMO system. This will increase the MIMO efficiency of the MIMO system; that is, the measured MIMO capacity for the real scenario can be close to the calculated MIMO capacity for the ideally rich multipath condition.

It is worth noting that nearby 100% MIMO efficiency in 4.8-4.9 GHz is obtained for the 8 × 4 MIMO system with the fabricated 8-port array studied here. As compared to the 16 × 8 MIMO system (16 receive antennas for 8 spatial streams) studied in the 7.1 GHz band (7.025-7.125 GHz), the MIMO efficiency is reported to be around 86%∼90% [8], [9]. Also

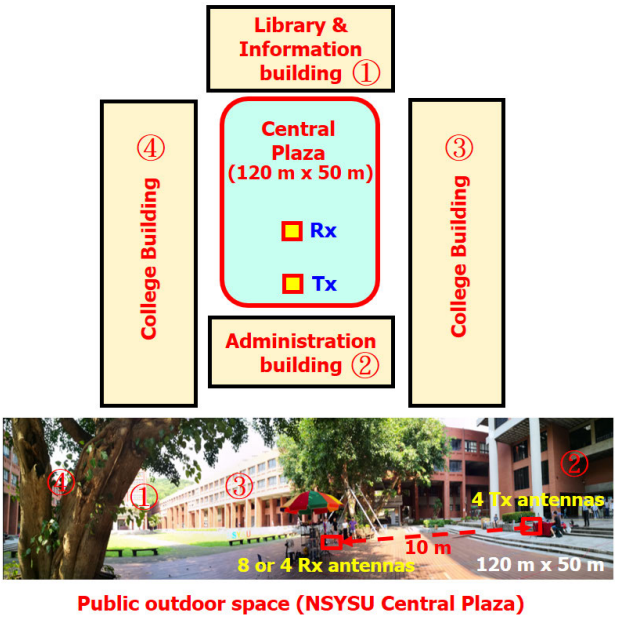

FIGURE 25. The public outdoor scenario in the NSYSU central plaza (area 120 m × 50 m) for the 8 × 4 and 4 × 4 MIMO systems testing.

note that the public indoor scenario in [8] and [9] is same as the testing scenario here.

Since the MIMO system with 8 spatial streams is more complex than that with 4 spatial streams, it is reasonable that better MIMO efficiency for the receive antennas two times the spatial streams is obtained here for the 8 × 4 MIMO system than for the 16 × 8 MIMO system in [8] and [9]. Additionally, in the same testing scenario, the lower

TABLE 3. Measur ed 8 × 4 and 4 × 4 MIMO system performance for the campus public outdoor scenario (Fig. 25).

f_0 = 4.85 GHz (4.8-4.9 GHz), Campus public outdoor space (120 m x 50 m), Rx/Tx distance 10 m		
MIMO system	8 x 4 MIMO	4 x 4 MIMO
Signal modulation	1024 QAM	64 QAM
Measured Signal Noise Ratio (dB) of 8 or 4 Rx antennas at the receiver side	Ports 1-8 of 8 Rx antennas 24.9, 28.4, 30.7, 25.6 31.6, 25.1, 29.7, 25.0 (Average SNR ≈ 28.4 dB)	Ports 1-4 of 8 Rx antennas 25.0, 32.7, 30.5, 26.6 (Average SNR ≈ 27.6 dB)
Calculated MIMO Capacity (A) (Ideally rich multipath condition)	39.4 bps/Hz	31.2 bps/Hz
Measured MIMO Capacity (B)	33.0 bps/Hz	25.6 bps/Hz
MIMO Efficiency (B/A)	83.8%	82.1%
Uncoded Bit Error Rate	0.045	0.023
Coded Bit Error Rate	0	0
Measured Throughput (T)	3135 Mbps	1924 Mbps
Spectral Efficiency (T/100 MHz)	31.35 bps/Hz	19.24 bps/Hz
Spectral efficiency per stream (public outdoor scenario)	7.84 bps/Hz	4.81 bps/Hz

frequencies (4.8-4.9 GHz here) usually have better multipath property than the higher frequencies (7.025-7.125 GHz [8], [9]). Thus, the MIMO system with 4 spatial streams and the lower frequencies in 4.8-4.9 GHz may account for the much better MIMO efficiency obtained here.

In this study, the bit error rate (BER) defined by the ratio of the erroneous data received at the receiver to the total transmitted data at the transmitter is low enough so that the coded BER is all zero for the two cases of 1024 AM and 4096 QAM. The zero coded BER indicates that the 8 × 4 MIMO system in the testing scenario supports the signal modulation of 1024 QAM and 4096 QAM.

The data throughput defined by the correct data received at the receiver reaches 3281 Mbps (1024 QAM) and 3897 Mbps (4096 QAM); and the corresponding spectral efficiency is 32.81 bps/Hz (1024 QAM) and 38.97 bps/Hz. Thus, the spectral efficiency per stream is 8.20 bps/Hz (1024 QAM) and 9.74 bps/Hz (4096 QAM). Note that, to our best knowledge, the latter with 9.74 bps/Hz stream is the highest for the MIMO system with 4 spatial streams that have been reported.

Additional testing of the MIMO system with 4 spatial streams in the campus outdoor scenario (area 120 m × 50 m) is conducted. The public outdoor scenario as shown in Fig. 25 is expected to have less or much less rich multipath propagation than the indoor scenario in Fig. 24. In addition, both the 8 × 4 and 4 × 4 MIMO systems are tested. For the 4 × 4 MIMO system, only Ports 1-4 of the fabricated 8-port array are used as 4 Rx antennas at the receiver.

Table 3 lists the measured 8 × 4 and 4 × 4 MIMO system performance for the public outdoor scenario (Fig. 25). The 8 or 4 Rx antennas face the 4 Tx antennas; and the distance between the Rx and Tx antennas is 10 meters. For the 8 × 4 MIMO system, it supports 1024 QAM with MIMO efficiency 83.8% (calculated MIMO capacity 39.4 bps/Hz, measured MIMO capacity 33.0 bps/Hz), uncoded BER 0.045, coded BER 0, measured data throughput 3135 Mbps, spectral efficiency 31.35 bps/Hz, and spectral efficiency per stream 7.84 bps/Hz.

For the 4 × 4 MIMO system, it supports only 64 QAM with MIMO efficiency 82.1% (calculated MIMO capacity 31.2 bps/Hz, measured MIMO capacity 25.6 bps/Hz), uncoded BER 0.023, coded BER 0, measured data throughput 1924 Mbps, spectral efficiency 19.24 bps/Hz, and spectral efficiency per stream 4.81 bps/Hz. Note that, the 4 × 4 MIMO system in the outdoor scenario cannot support the signal modulation of 256 QAM and 1024 QAM (their uncoded BER all larger than 0.1).

In the outdoor scenario in which the multipath propagation is generally not as rich as in the indoor scenario, large effects of using additional 4 Rx antennas for the 8 × 4 MIMO system are observed. The obtained spectral efficiency per spatial stream is 7.84 bps/Hz, much larger than that (4.81 bps/Hz) obtained for the 4 × 4 MIMO system with 4 Rx antennas only. The results suggest that the effects of applying more Rx antennas in the scenario with less rich multipath condition will be more prominent. The obtained results also indicate the

capability of the proposed 8-port 2 × 2 DPP antenna array for practical MIMO system applications.

It is also worth noting that the better MIMO performance obtained here may also be attributed to the proposed 8-port 2 × 2 DPP antenna array showing no prominent antenna gain as compared to that in [7]. This is expected to lead to relatively richer multipath propagation for the MIMO system, thereby obtaining high data throughput and spectral efficiency per stream.

VI. CONCLUSION

A compact 8-port 2 × 2 DPP antenna array with modified cavity field distribution for enhanced port isolation has been proposed for IoT or XR device MIMO antenna applications in the 5G n79 band (4.4-5.0 GHz). The operating principle and design consideration of the compact 8-port array and the DPP antenna therein have been addressed. The compact array has also been experimentally studied. We further apply the fabricated array as 8 receive antennas in the 8 × 4 MIMO system with 4 spatial streams in campus public indoor and outdoor scenarios to test its capability for MIMO system applications. A high data throughput of 3.897 GHz for the 8 × 4 MIMO system (an ERA-aided MIMO with receive antennas two times that of the spatial streams) tested in 4.8-4.9 GHz has been obtained. The high data throughput indicates that the spectral efficiency per stream is as high as 9.74 bps/Hz, which to our best knowledge is the highest for the MIMO system with 4 spatial streams that have been reported. The results support that the compact 8-port array is promising for practical MIMO system applications; and additionally, the 8 × 4 MIMO system will be attractive for high data throughput applications. Furthermore, for future or 6G (six-generation) communications, the MIMO system will be very likely to support 8 spatial streams [4], two times the 4 streams for 5G communications. In this case, in order to obtain enhanced data throughput or spectral efficiency for such future MIMO systems, the receive antennas for the IoT device should also outnumber the spatial streams as indicated in this study; for example, 16 receive antennas for 8 spatial streams (the 16 × 8 MIMO system) for future MIMO systems. For such applications, one can use two of the proposed 8-port 2 × 2 DPP array to conveniently obtain 16 receive antennas for the IoT devices. That is, the proposed compact 8-port array is also expected to find applications in future or 6G communications.

REFERENCES

[1] Int. Telecommun. Union. (Dec. 16, 2023). *World Radiocommunication Conference (WRC-23) Provisional Final Acts*. [Online]. Available: https://www.itu.int/wrc-23/

[2] (Aug. 08, 2022). *Adding Channel Bandwidth to Existing NR Bands*. [Online]. Available: https://www.3gpp.org/technologies/adding-channel-bandwidth-to-existing-nr-bands

[3] I. R. R. Barani, K.-L. Wong, Y.-X. Zhang, and W.-Y. Li, "Low-profile wideband conjoined open-slot antennas fed by grounded coplanar waveguides for 4×4 G MIMO operation," *IEEE Trans. Antennas Propag.*, vol. 68, no. 4, pp. 2646–2657, Apr. 2020.

[4] (Jan. 7, 2022). *MediaTek 6G Vision Whitepaper*. [Online]. Available: https://www.mediatek.com/whitepapers/6g

[5] K.-L. Wong, H.-C. Kao, and W.-Y. Li, "Wideband low-profile eight-port eight-wave annular-ring patch antenna based on using eight dual-shorted dual-resonant ring sectors for 8×8 MIMO mobile devices," *IEEE Access*, vol. 11, pp. 18–32, 2023.

[6] K.-L. Wong, Y.-R. Chen, and W.-Y. Li, "Eight-Planar-Monopole MIMO circular array generating eight uncorrelated waves for 6G upper mid-band 8×8 MIMO access points," *IEEE Access*, vol. 11, pp. 68018–68030, 2023.

[7] K.-L. Wong, T.-C. Wei, Y.-S. Tseng, and W.-Y. Li, "Compact 2×2 dual-polarized patch antenna array transmitting eight uncorrelated waves for the WiFi-6E MIMO access point featuring eight spatial streams," *IEEE Access*, vol. 12, pp. 36793–36809, 2024.

[8] K.-L. Wong, S.-E. Hong, Y.-S. Tseng, and W.-Y. Li, "Low-profile compact 8-Port MIMO antenna module and its 1×2 array for 6G 16×8 device MIMO application," *IEEE Access*, vol. 11, pp. 137011–137024, 2023.

[9] K.-L. Wong, S.-E. Hong, and W.-Y. Li, "Low-profile four-port MIMO antenna module based 16-port closely-spaced 2× 2 module array for 6G upper mid-band mobile devices," *IEEE Access*, vol. 11, pp. 110796–110808, 2023.

[10] M. Chung and W. Chang, "Low-cost, low-profile and miniaturized single-plane antenna design for an Internet of Thing device applications operating in 5G, 4G, V2X, DSRC, WiFi 6 band, WLAN, and Wimax communication systems," *Microw. Opt. Technol. Lett.*, vol. 62, no. 4, pp. 1765–1773, Apr. 2020.

[11] (May 20, 2022). *NVIDIA: What is Extended Reality?*. [Online]. Available: https://blogs.nvidia.com/blog/what-is-extended-reality/

[12] (Sep. 17, 2023). *Expand Reality: 8 Upcoming XR Devices for Enterprise and Entertainment*. [Online]. Available: https://www.expandreality.io/8-upcoming-xr-devices-for-enterprise-and-entertainment

[13] Y.-M. Zhang, S. Zhang, J.-L. Li, and G. F. Pedersen, "A transmission-line-based decoupling method for MIMO antenna arrays," *IEEE Trans. Antennas Propag.*, vol. 67, no. 5, pp. 3117–3131, May 2019.

[14] T. A. Elwi, F. Taher, B. S. Virdee, M. Alibakhshikenari, I. J. Garcia Zuazola, A. Krasniqi, A. Shibib Kamel, N. Türker Tokan, S. Khan, N. O. Parchin, P. Livreri, I. Dayoub, G. Pau, S. Aïssa, E. Limiti, and M. F. A. Sree, "On the performance of a photonic reconfigurable electromagnetic band gap antenna array for 5G applications," *IEEE Access*, vol. 12, pp. 60849–60862, 2024.

[15] S. Hassan Ghadeer, S. Kamal Abd. Rahim, and T. A. Elwi, "Ultra-wideband MIMO antenna array for mm-wave 5G applications," in *Proc. IEEE Int. Symp. Antennas Propag. (ISAP)*, Nov. 2023, pp. 1–2.

[16] M. Li, Y. Zhang, D. Wu, K. L. Yeung, L. Jiang, and R. Murch, "Decoupling and matching network for dual-band MIMO antennas," *IEEE Trans. Antennas Propag.*, vol. 70, no. 3, pp. 1764–1775, Mar. 2022.

[17] M. Li, Y. Zhang, F. Jiang, D. Wu, K. L. Yeung, L. Jiang, and R. Murch, "Improvement for MIMO systems by increasing antenna isolation and shaping radiation pattern using hybrid network," *IEEE Trans. Ind. Electron.*, vol. 69, no. 12, pp. 13891–13901, Dec. 2022.

[18] K.-L. Wong, M.-F. Jian, C.-J. Chen, and J.-Z. Chen, "Two-port same-polarized patch antenna based on two out-of-phase TM10 modes for access-point MIMO antenna application," *IEEE Antennas Wireless Propag. Lett.*, vol. 20, pp. 572–576, 2021.

[19] (Mar. 1, 2022). *3D High Frequency Electromagnetic Simulation Software, ANSYS HFSS*. [Online]. Available: https://www.ansys.com/products/electronics/ansys-hfss

[20] K.-L. Wong, C.-J. Chen, and W.-Y. Li, "Integrated four low-profile shorted patch dual-band WLAN MIMO antennas for mobile device applications," *IEEE Trans. Antennas Propag.*, vol. 69, no. 6, pp. 3566–3571, Jun. 2021.

[21] K.-L. Wong, M.-F. Jian, and W.-Y. Li, "Low-profile wideband four-corner-fed square patch antenna for 5G MIMO mobile antenna application," *IEEE Antennas Wireless Propag. Lett.*, vol. 20, pp. 2554–2558, 2021.

[22] K.-L. Wong, C.-J. Ho, and W.-Y. Li, "Low-profile six-port circular patch antenna with six triple-shorted dual-resonant 60°-disk sectors to generate six uncorrelated waves for wideband mobile MIMO antennas," *IEEE Access*, vol. 10, pp. 80277–80288, 2022.

[23] J.-S. Row, S.-H. Yeh, and K.-L. Wong, "Compact dual-polarized microstrip antennas," *Microw. Opt. Technol. Lett.*, vol. 27, no. 4, pp. 284–287, Nov. 2000.

[24] K.-L. Wong, S.-W. Su, and Y.-L. Kuo, "A printed ultra-wideband diversity monopole antenna," *Microw. Opt. Technol. Lett.*, vol. 38, no. 4, pp. 257–259, Aug. 2003.

[25] A. Iqbal, A. Altaf, M. Abdullah, M. Alibakhshikenari, E. Limiti, and S. Kim, "Modified U-shaped resonator as decoupling structure in MIMO antenna," *Electronics*, vol. 9, no. 8, p. 1321, Aug. 2020.

[26] Y. Okano and K. Cho, "Antenna measurement system for mobile terminals," *NTT DoCoMo Tech. J.*, vol. 9, no. 2, pp. 43–50, 2007.
[27] K.-L. Wong, X.-Q. Ye, and W.-Y. Li, "Wideband four-port single-patch antenna based on the quasi-TM1/2,1/2 mode for 5G MIMO access-point application," *IEEE Access*, vol. 10, pp. 9232–9240, 2022.
[28] (Dec. 6, 2019). *DIGITIMES Asia: Taiwan Assigns 4.8–4.9GHz As Dedicated 5G Band for Special Purposes*. [Online]. Available: https://www.digitimes.com/news/a20191206PD215.html

KIN-LU WONG (Fellow, IEEE) received the B.S. degree in electrical engineering from National Taiwan University, Taipei, Taiwan, in 1981, and the M.S. and Ph.D. degrees in electrical engineering from Texas Tech University, Lubbock, TX, USA, in 1984 and 1986, respectively.

From 1986 to 1987, he was a Visiting Scientist with the Max-Planck-Institute for Plasma Physics, Munich, Germany. Since 1987, he has been with the Electrical Engineering Department, National Sun Yat-sen University (NSYSU), Kaohsiung, Taiwan, where he became a Professor in 1991. From 1998 to 1999, he was a Visiting Scholar with the ElectroScience Laboratory, The Ohio State University, Columbus, OH, USA. He was elected to be a Sun Yat-sen Chair Professor and a Distinguished Chair Professor with NSYSU, in 2005 and 2017, respectively; a Distinguished Researcher with the National Science and Technology Council of Taiwan, in 2012; and the National Chair Professor and the Lifetime National Chair Professor of the Ministry of Education (MOE), Taiwan, in 2016 and 2023, respectively. He was also the Chairperson of the Electrical Engineering Department, from 1994 to 1997; the Vice President of Research Affairs, from 2005 to 2007; and the Senior Vice President with NSYSU, from 2007 to 2012. He is currently the Director of the 6G Communication and Sensing Research Center, funded by the MOE. He has authored more than 590 refereed journal articles and 300 conference articles and has personally supervised 57 graduated Ph.D.'s. He holds over 300 patents, including 106 U.S. patents. He is the author of *Design of Nonplanar Microstrip Antennas and Transmission Lines* (Wiley, 1999), *Compact and Broadband Microstrip Antennas* (Wiley, 2002), and *Planar Antennas for Wireless Communications* (Wiley, 2003). His published articles have been cited over 36,600 times with an H-index of 89 in Google Scholar.

Dr. Wong served as an IEEE AP-S AdCom Member, an IEEE TRANSACTIONS ON ANTENNAS AND PROPAGATION (IEEE TAP) Track Editor/an Associate Editor, an IEEE TRANSACTIONS ON ANTENNAS AND PROPAGATION (IEEE TAP) Paper Awards Committee Member, and an AP-Society Field Awards Committee Member. He was also a PE7 Panel Member of European Research Council Advanced Grant Panel, in 2015, 2017, and 2019; and a Chief Consultant of the Institute of Antenna Engineers of Taiwan. He received the Outstanding Research Award (three times) from Taiwan National Science Council, in 1995, 2000, and 2002. He also received the Outstanding Electrical Engineering Professor Award from the Institute of Electrical Engineers of Taiwan, in 2003, and the Outstanding Engineering Professor Award from the Institute of Engineers of Taiwan, in 2004. In 2008, the research achievements on handheld device antennas of NSYSU Antenna Laboratory led by him was selected to be top 50 scientific achievements of Taiwan Ministry of Science and Technology in past 50 years (1959–2009). He was a recipient of the 2010 Outstanding Research Award of Pan Wen Yuan Foundation and selected as top 100 Honor of Taiwan by Global Views Monthly, in 2010, for his contribution in mobile antenna research. He was also a recipient of the Academic Award from Taiwan Ministry of Education, in 2012. He and his graduate students received the Best Paper Award (APMC Prize) from 2008 APMC; and the Best Student Paper Award/Young Scientist Award from 2007 ISAP, 2008 APMC, 2009 ISAP, 2010 ISAP, 2012 ISAP, and 2016 ISAP. His graduate students also won the first prize of 2007 and 2009 Taiwan National Mobile Handset Antenna Design Competition. He was awarded the Best Associate Editor two times (2015 and 2016) of IEEE TRANSACTIONS ON ANTENNAS AND PROPAGATION. He also served as the Chair for the Judge Panel of the National Communication Antenna Design Competition organized by Taiwan Ministry of Economics, from 2014 to 2024. He served as the General Chair for 2012 APMC, 2014 ISAP, and 2016 APCAP held at Kaohsiung, Taiwan; and also served as the Honorary General Chair for 2023 APMC held at Taipei, Taiwan. He was elected as a Thomson Reuters Highly Cited Researcher in both 2014 and 2015 and an Elsevier Most Cited Researcher, in 2015. In 2022, he was selected by Research.com to be ranked #99 in Full World Ranking and #1 in Full Taiwan Ranking in the 2022 Edition of Ranking of Top 1000 Scientists in the field of Electronics and Electrical Engineering.

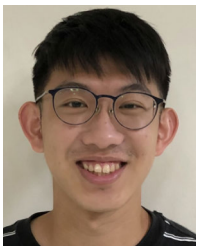

YI-YANG HUANG (Student Member, IEEE) received the B.S. degree in electrical engineering from Yuan Ze University, Taoyuan, Taiwan, in 2022. He is currently pursuing the M.S. degree with National Sun Yat-sen University, Kaohsiung, Taiwan. His research interests include the high-density MIMO antennas for Internet of Things (IoT) devices, mobile devices, and access points for 5G/6G mobile communication services.

WEI-YU LI (Member, IEEE) was born in Taipei, Taiwan, in 1981. He received the B.S. degree in electrical engineering from Feng Chia University, Taichung, Taiwan, in 2004, and the M.S. and Ph.D. degrees in electrical engineering from National Sun Yat-sen University (NSYSU), Kaohsiung, Taiwan, in 2006 and 2009, respectively.

After graduated from NSYSU, in 2009, he has been with the Information and Communication Research Laboratories (ICL) of Industrial Technology Research Institute (ITRI), Hsinchu, Taiwan, participating and leading advanced research for development of emerging wireless antenna technologies. From April 2012 to October 2012, he was an Exchange Guest Researcher with the National Institute of Information and Communications Technology (NICT), Tokyo, Japan. He is currently the Technology Manager of ITRI. He has authored or coauthored 35 refereed journal articles and 40 conference articles. He holds over 70 patents, including U.S., Taiwan, China, and EU patents. His published articles have been cited over 1,850 times with a H-index of 24 in Google Scholar.

Dr. Li served as an International Steering Committee Member for ISAP, from 2019 to 2022; and an AdCom Member for the Institute of Antenna Engineers of Taiwan, from 2014 to 2015 and from 2018 to 2023. He also served as a member for the Judge Panel of the National Terminal Antenna Design Competition, organized by the Taiwan Ministry of Economics, from 2014 to 2024. He received the Young Scientist Award, in 2007, ISAP and the Best Paper Award (APMC Prize), in 2008, APMC. He has been a principal investigator or a co-principal investigator of many research projects in ITRI and has received numerous recognitions, including the First Prize of the Outstanding Research Award of ITRI, in 2010; the Solar Industrial Award (SIA) of Europe, in 2011; the Outstanding Innovation Award of ITRI, in 2013; the Second Prize of the Outstanding Research Award of ITRI, in 2014; the 2015 Research and Development 100 Award Finalist of the U.S.; the Outstanding Innovation Award of ITRI, in 2017; the First Prize of the Outstanding Industrialization Award of ITRI, in 2017; the Second Prize of the Outstanding Industrialization Award of ITRI, in 2020; the Third Prize of the Outstanding Industrialization Award of ITRI, in 2021; and the First Prize of the Outstanding Research Award of ITRI, in 2024. He also received the Outstanding Lecturer Award of ITRI, in 2013; the International Paper Award of ICL of ITRI, in 2020; and the Annual Paper Award of ITRI, in 2023. He also served as the Chair for IEEE AP-S Tainan Chapter, from 2021 to 2022.